



Gallium Arsenide detectors for X-ray and electron (beta particle) spectroscopy



G. Lioliou*, A.M. Barnett

Semiconductor Materials and Devices Laboratory, Sch. of Engineering and Informatics, University of Sussex, Falmer, Brighton BN1 9QT, UK

ARTICLE INFO

Article history:

Received 17 June 2016

Received in revised form

22 August 2016

Accepted 22 August 2016

Available online 23 August 2016

Keywords:

Gallium Arsenide

P-i-n photodiodes

X-ray spectroscopy

Beta particle spectroscopy

ABSTRACT

Results characterizing GaAs p^+i-n^+ mesa photodiodes with a $10\ \mu\text{m}$ i layer for their spectral response under illumination of X-rays and beta particles are presented. A total of 22 devices, having diameters of $200\ \mu\text{m}$ and $400\ \mu\text{m}$, were electrically characterized at room temperature. All devices showed comparable characteristics with a measured leakage current ranging from $4\ \text{nA}/\text{cm}^2$ to $67\ \text{nA}/\text{cm}^2$ at an internal electric field of $50\ \text{kV}/\text{cm}$. Their unintentionally doped i layers were found to be almost fully depleted at $0\ \text{V}$ due to their low doping density. ^{55}Fe X-ray spectra were obtained using one $200\ \mu\text{m}$ diameter device and one $400\ \mu\text{m}$ diameter device. The best energy resolution ($FWHM$ at $5.9\ \text{keV}$) achieved was $625\ \text{eV}$ using the $200\ \mu\text{m}$ and $740\ \text{eV}$ using the $400\ \mu\text{m}$ diameter device, respectively. Noise analysis showed that the limiting factor for the energy resolution of the system was the dielectric noise; if this noise was eliminated by better design of the front end of the readout electronics, the achievable resolution would be $250\ \text{eV}$. ^{63}Ni beta particle spectra obtained using the $200\ \mu\text{m}$ diameter device showed the potential utility of these detectors for electron and beta particle detection. The development of semiconductor electron spectrometers is important particularly for space plasma physics; such devices may find use in future space missions to study the plasma environment of Jupiter and Europa and the predicted electron impact excitation of water vapor plumes from Europa hypothesized as a result of recent Hubble Space Telescope (HST) UV observations.

© 2016 The Authors. Published by Elsevier B.V. This is an open access article under the CC BY license (<http://creativecommons.org/licenses/by/4.0/>).

1. Introduction

Gallium Arsenide has been the subject of much interest for its use in photon counting X-ray spectroscopic detector systems. As a wide bandgap material ($1.42\ \text{eV}$ [1]), the resulting low thermally generated leakage current density allows its use at room and high temperatures with less degradation in energy resolution compared to traditional narrower bandgap materials such as Si and Ge [2]. Another advantage of GaAs is its relatively low electron–hole pair creation energy ($4.184\ \text{eV}$ [1]) compared to other wide bandgap materials. Furthermore, GaAs has been proven to be more radiation resistant than Si for electrons [3], γ -rays [4] and low energy hadrons [5]. Moreover, high detection efficiency per unit thickness is achieved with GaAs due to its high effective atomic number.

As a result, GaAs can be used for radiation detection in harsh environments (high temperature and intense radiation environment) without the need for cooling and shielding, and with good energy resolution [2]. The elimination of the cooling and shielding system can lead to the reduction of the mass, cost, volume and

power of the total detection system. Space missions and terrestrial applications with such restrictions could benefit from the use of GaAs. Some examples include X-ray fluorescence spectroscopy missions to Mercury [6] and Jupiter [7] and X-ray fluorescence spectrometry in industrial process control applications. The use of radiation hard GaAs detectors may also be particularly beneficial for future missions to the intense radiation environment of Jupiter and its moons (doses of as high as $6\ \text{MRad}$ [8]).

Another potential application of GaAs photodiodes is the in situ low energy ($1\text{--}100\ \text{keV}$) electron spectroscopy at Europa along with contemporaneous UV imaging from either an orbiter or the Hubble Space Telescope (HST) which would allow direct observational data gathering to test predictions that electron impact excitation of water vapor plumes explains the auroral observations at Europa's polar regions in 2012 [9]. Although electron spectroscopy can also be realized with scintillators [10,11], semiconductor detectors are of a great advantage in many electron detection applications. Poorer energy resolution is achieved using scintillators than using semiconductor detectors [10,12]. The lower energy needed to produce an electron–hole pair in a semiconductor (e.g., $4.184\ \text{eV}$ for GaAs [1]) than the energy needed to produce a photoelectron ejection in a scintillation/photomultiplier tube ($\geq 100\ \text{eV}$) results in better statistics (production of more charge

* Corresponding author.

carriers from the primary ionization effect) and hence in energy resolution improvement of semiconductor detectors compared to scintillators [13]. Electron spectrometers have also been realized using microchannel plate (MCP) detectors, which have been proven to be useful devices in space applications (e.g. the Electron Spectrometer in the Cassini Plasma Spectrometer for the exploration of the Saturn system [14]). An alternative to MCP detectors is charge coupled devices (CCD) for the direct detection of electrons without the need of high voltages and high vacuums required in MCP detectors [15]. Langmuir probes are also used for electron detection (e.g. in measuring the electron energy distribution functions in plasmas [16]).

Results characterizing GaAs planar p^+-i-n^+ diodes with Schottky contacts and guard rings in a 5×5 array structure with low dark current densities ($< 6 \text{ nA/cm}^{-2}$ at room temperature) coupled to ultra low noise front end electronics was reported in Ref. [17]. The best energy resolution achieved with these devices was 266 eV at 5.9 keV at room temperature and has not yet been replicated. Similar structure and thicker devices in a 32×32 pixel array form were reported in Ref. [18] with an energy resolution of 300 eV at 5.9 keV at room temperature. GaAs p^+-i-n^+ mesa X-ray photodiodes have been characterized for X-ray ($2 \mu\text{m}$ [19], $3 \mu\text{m}$ [20] and $7 \mu\text{m}$ [21,22] i layer thickness) and β^- particle spectroscopy ($2 \mu\text{m}$ i layer thickness [23]). Research has also been conducted on the use of GaAs p^+-i-n^+ mesa X-ray photodiodes as X-ray photovoltaic batteries [24].

In this paper, results from randomly selected fully etched GaAs p^+-i-n^+ mesa X-ray photodiodes with $10 \mu\text{m}$ thick i layers are presented. These are the thickest GaAs p^+-i-n^+ mesa X-ray photodiodes reported in the literature to date. 22 devices of two different diameters ($200 \mu\text{m}$ and $400 \mu\text{m}$) are electrically characterized and reported. Following this, one representative device of each diameter is characterized as an X-ray photon counting spectroscopic detector. Accumulated ^{55}Fe spectra are presented and the noise of the system is analyzed. Finally, results are reported using one $200 \mu\text{m}$ diameter device for ^{63}Ni β^- spectroscopy and its suitability in β^- particle and electron detection is discussed.

2. Device structure

The GaAs p^+-i-n^+ mesa photodiodes were grown and fabricated to the Authors' specifications at the EPSRC National Centre for III-V Technologies, Sheffield, UK. GaAs epilayers were grown on a commercial GaAs n^+ substrate by metalorganic vapor phase epitaxy. The unintentionally doped i layer had a thickness of $10 \mu\text{m}$. The resulting wafer structure is summarized in Table 1. Mesa diodes with diameters of $200 \mu\text{m}$ and $400 \mu\text{m}$ were chemically etched using a $1:1:1 \text{ H}_3\text{PO}_4:\text{H}_2\text{O}_2:\text{H}_2\text{O}$ solution followed by 10 s in a $1:8:80 \text{ H}_2\text{SO}_4:\text{H}_2\text{O}_2:\text{H}_2\text{O}$ solution. The top Ohmic contact consisted of 20 nm of Ti and 200 nm of Au. It covered 45% of the surface of the $200 \mu\text{m}$ diameter devices and the 33% of the $400 \mu\text{m}$

Table 1
GaAs p^+-i-n^+ mesa photodiodes layer structure.

Material	Type	Thickness (nm)	Doping density (cm^{-3})
Ti		20	
Au		200	
GaAs	p^+	500	2×10^{18}
GaAs	i	10,000	Undoped
GaAs	n^+	1000	2×10^{18}
GaAs	n^+ substrate		
Au		200	
InGe		20	

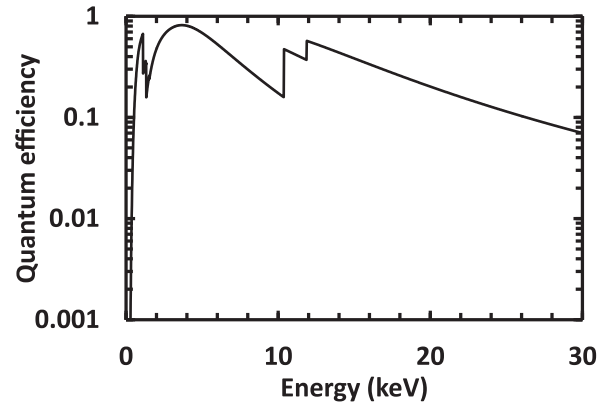


Fig. 1. Calculated X-ray quantum efficiency of the GaAs p^+-i-n^+ mesa photodiodes as a function of X-ray photon energy.

diameter devices. The rear Ohmic contact consisted of 20 nm of InGe and 200 nm of Au. The GaAs devices were unpassivated.

The quantum efficiency of the devices for X-ray photons up to 30 keV was calculated and can be seen in Fig. 1. As a cautious assumption, to prevent over estimation of the quantum efficiency, the whole of the p^+ layer was assumed to be a dead region and only the i layer was assumed to be the active region of the devices.

3. Electrical characterization

Electrical characterization of 22 GaAs mesa p^+-i-n^+ photodiodes was performed under dark conditions at room temperature. There were 14 diodes with $200 \mu\text{m}$ diameter and 8 diodes with $400 \mu\text{m}$ diameter.

3.1. Current–voltage measurements

Dark current measurements as functions of both forward and reverse applied voltage (I - V characteristics) were performed using a Keithley 6487 Picoammeter/Voltage Source. The dark current was measured as a function of forward bias from 0 V to 1 V and as a function of reverse bias from 0 V to 50 V at room temperature. Fig. 2 shows the measured currents, I_F , as a function of applied forward bias, V_F , of representative $200 \mu\text{m}$ and $400 \mu\text{m}$ diameter devices.

The saturation current, I_0 , and the ideality factor, n , were extracted for each device based on the linear region of their semi-logarithm dark current as a function of forward bias [22]. The saturation current, I_0 , was found to vary from $3 \times 10^{-13} \text{ A}$ to

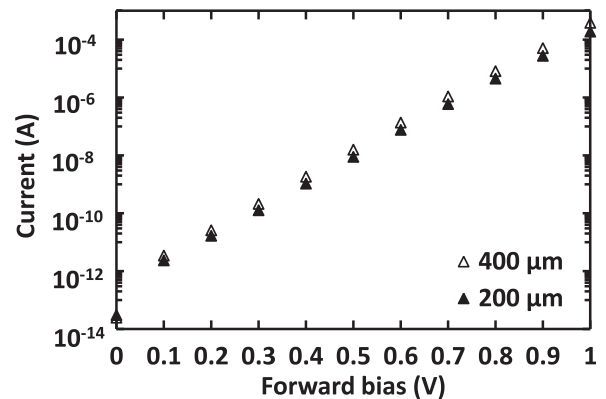


Fig. 2. Dark current as a function of applied forward bias for a $200 \mu\text{m}$ (filled triangles) and $400 \mu\text{m}$ (open triangles) diameter GaAs p^+-i-n^+ photodiode at room temperature.

7×10^{-13} A among different devices at room temperature with a mean of $(5 \pm 1) \times 10^{-13}$ A (rms deviance). The ideality factor, n , was found to vary from 1.89 to 1.99 among different devices with a mean of 1.95 ± 0.02 . The calculated ideality factor values (≈ 2) suggest that the recombination current dominates [25]. Temperature dependent dark current measurements as functions of applied forward bias would help to identify the contribution of tunneling on the conduction process as well as the conduction mechanism at high temperatures. Although the area of the 400 μm diameter devices is four times larger than the area of the 200 μm diameter devices, the 400 μm diameter devices' dark currents at 1 V forward bias were found to be only two times greater than the dark current of the 200 μm devices. The dark current at 1 V applied forward bias was measured to be $(2.0 \pm 0.1) \times 10^{-4}$ A for the 200 μm diameter devices and $(4.0 \pm 0.2) \times 10^{-4}$ A for the 400 μm diameter devices. The dark forward current scaled with perimeter of the devices, rather than their area which suggested that the surface leakage component was not negligible and that future devices may benefit from surface passivation.

The measured dark currents, I_R , as a function of applied reverse bias, V_R , of a representative 200 μm and a 400 μm diameter device are shown in Fig. 3. All GaAs p^+-i-n^+ photodiodes showed low leakage current densities at a mean electric field of 50 kV/cm across the i region (-50 V reverse bias) at room temperature: the measured leakage current density was found to vary from 13 nA/cm² to 67 nA/cm² with an average of (40 ± 16) nA/cm² among the 200 μm and from 4 nA/cm² to 21 nA/cm² with an average of (13 ± 6) nA/cm² among the 400 μm diameter devices, at 50 kV/cm. For comparison purposes, the leakage current densities at an electric field of 22 kV/cm are also reported: they were found to vary from 10 nA/cm² to 40 nA/cm² with an average of (24 ± 7) nA/cm² among the 200 μm and from 4 nA/cm² to 9 nA/cm² with an average of (7 ± 2) nA/cm² among the 400 μm diameter devices. These values are comparable with other high quality GaAs p^+-i-n^+ photodiodes previously reported e.g., ~ 10 nA/cm² [2], 17.4 nA/cm² and 1.08 nA/cm² [21], from 20 nA/cm² to 100 nA/cm² [26], at room temperature and at an electric field of 22 kV/cm.

The leakage current density at an electric field of 50 kV/cm and at room temperature, for all devices can be seen in Fig. 4. The 400 μm diameter devices showed lower leakage current densities than the 200 μm diameter devices at 50 kV/cm, suggesting that the leakage current did not scale with the junction area. This was attributed to the surface leakage current not being negligible as in Ref. [27], due to the devices being unpassivated. The separation of the bulk and surface components of the leakage current can be

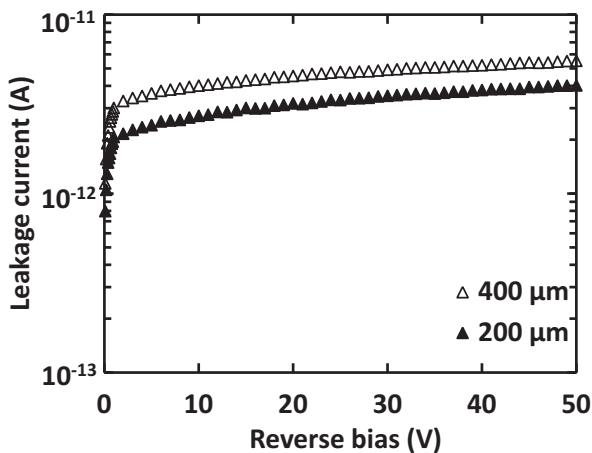


Fig. 3. Dark current as a function of applied reverse bias for representative 400 μm (open triangles) and 200 μm (filled triangles) diameter GaAs p^+-i-n^+ photodiodes at room temperature.

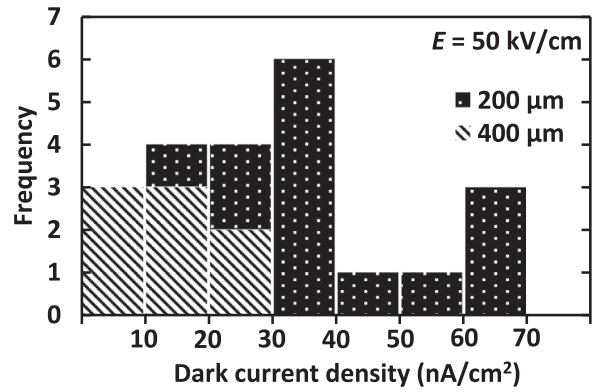


Fig. 4. Histogram of the dark current density of the 200 μm (black) and 400 μm (gray) diameter GaAs p^+-i-n^+ photodiodes at an electric field of 50 kV/cm a.

achieved with dark current measurements on different diameter devices and the effect of the passivation to surface leakage current can be investigated with measurements on devices with different passivation materials. Future measurements can also include temperature dependent dark current measurements as functions of applied reverse bias to find the prevailing reverse conduction mechanism (generation, diffusion and tunneling) of the devices as a function of temperature [22].

3.2. Capacitance–voltage measurements

To determine the depletion width and the doping concentrations in the intrinsic layer of the GaAs p^+-i-n^+ devices, the devices' capacitances were measured as functions of applied forward and reverse bias, at room temperature. The capacitances were measured using an HP 4275 A Multi Frequency LCR meter whose test signal was sinusoidal with a 50 mV rms magnitude and 1 MHz frequency. The capacitance of the empty packages was determined by measuring the capacitance between the common pin (GND) and 17 pins with no diode connected. It was found to vary from 0.71 pF to 0.81 pF with the average value, (0.78 ± 0.02) pF, being subtracted from the total measured capacitance. The resulting capacitance, the p^+-i-n^+ junction capacitance, as a function of applied forward bias of representative 200 μm and 400 μm diameter devices is presented in Fig. 5.

The junction capacitance was mostly defined by the diffusion capacitance, $C_D(V_F)$, at forward applied biases [25]. The junction capacitance was found to increase by (7.7 ± 0.8) pF for the 400 μm diameter devices and by (3.5 ± 0.7) pF for the 200 μm diameter

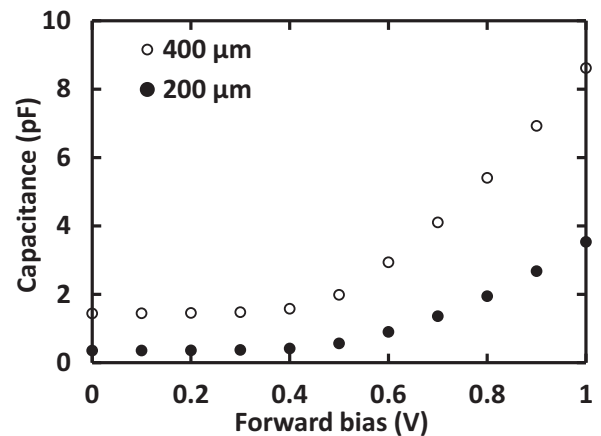


Fig. 5. Dark capacitance as a function of applied forward bias for a 200 μm (filled circles) and 400 μm (open circles) diameter GaAs p^+-i-n^+ photodiode at room temperature.

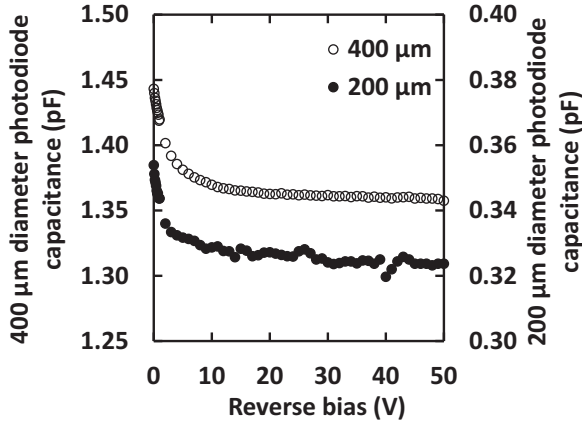


Fig. 6. Dark capacitance as a function of applied reverse bias for a 200 μm (filled circles) and 400 μm (open circles) diameter GaAs p^+-i-n^+ photodiode at room temperature.

devices, as the applied bias increased from 0 V to +1 V. Assuming there was zero diffusion capacitance at 0 V, it may be said that there was (7.7 ± 0.8) pF diffusion capacitance for the 400 μm diameter devices and (3.5 ± 0.7) pF diffusion capacitance for the 200 μm diameter devices, at +1 V forward applied bias. The ratio of the diffusion capacitance of the 400 μm devices over the diffusion capacitance of the 200 μm diameter devices ($=2.1 \pm 0.5$), at +1 V is in accordance with the ratio of the forward dark current of the 400 μm diameter devices over the forward dark current of the 200 μm diameter devices ($=2$), at +1 V which was expected since the diffusion capacitance is directly proportional to the forward dark current [25].

The measured capacitance as a function of applied reverse bias of representative 200 μm and 400 μm diameter devices can be seen in Fig. 6. The junction capacitance was mostly defined by the depletion layer capacitance, $C_{DL}(V_R)$, at reverse biases [25]. The depletion layer capacitance was found to decrease from (1.45 ± 0.03) pF at 0 V to (1.36 ± 0.03) at -50 V for the 400 μm diameter devices and from (0.35 ± 0.03) pF at 0 V to (0.32 ± 0.03) at -50 V for the 200 μm diameter devices. The variation of the capacitance (± 0.03 pF) among different devices at the same applied bias is in agreement with the total uncertainty in the capacitance measurements (± 0.03 pF).

The depletion layer width of the diodes as a function of applied reverse voltage, $W(V_R)$, was computed using the measured depletion layer capacitance, $C_{DL}(V_R)$, where

$$C_{DL}(V_R) = \frac{\epsilon_0 \epsilon A}{W(V_R)} \quad (1)$$

and ϵ_0 is the permittivity of free space, ϵ is the dielectric constant of GaAs and A is the area of the device [25]. The calculated depletion width of a representative 200 μm diameter device is presented in Fig. 7. Once the lightly doped intrinsic layer is fully depleted, the capacitance is independent of the applied reverse bias. All the diodes were almost fully depleted at 0 V. More specifically, the depletion widths of the 400 μm diameter devices were found to increase by an average of (0.68 ± 0.04) μm from (9.9 ± 0.2) μm at 0 V to (10.6 ± 0.2) μm at 50 V. The depletion widths of 13 out of 14 200 μm diameter devices were found to increase by (1.0 ± 0.2) μm from an average of (10 ± 1) μm at 0 V to (11 ± 1) μm at 50 V. The standard deviation (rms deviance) of the depletion widths of the 400 μm and 200 μm diameter devices were in agreement with the uncertainty of the depletion width for each diode calculated based on the total uncertainty in the capacitance measurements (± 0.03 pF). One of the 200 μm diameter devices had an apparent depletion width of (11 ± 1) μm at 0 V increasing

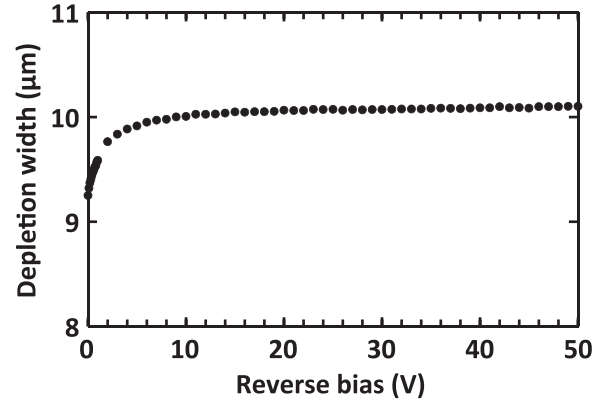


Fig. 7. Depletion width for a representative 200 μm diameter GaAs p^+-i-n^+ photodiode calculated from capacitance measurements as a function of applied reverse bias at room temperature.

to an apparent width of (14 ± 2) μm at 50 V. This result is unlikely to have been due to variations in the i layer thickness; instead it is more likely to have been a consequence of this device having a packaging capacitance of 0.7 pF rather than the mean value of 0.78 pF. With the assumption of a 0.7 pF packaging capacitance, this device's depletion width became identical to all other devices.

The carrier concentration as a function of distance below the p^+-i junction of the i layer was calculated based on the capacitance measurements, using the equation for general nonuniform distributions [25]. Fig. 8 shows the calculated carrier concentration of a representative 200 μm diameter device based on the data of Fig. 7.

Since the calculated carrier concentration was based on the capacitance measurements as functions of reverse bias (depletion layer capacitance), carrier concentration calculations can only be computed accurately at deep distances (close to the $i-n^+$ junction). The doping level of the i layer increased from $(2.8 \pm 0.9) \times 10^{14} \text{ cm}^{-3}$ to $(13 \pm 5) \times 10^{16} \text{ cm}^{-3}$ among the 400 μm diameter devices and from $(0.8 \pm 0.4) \times 10^{14} \text{ cm}^{-3}$ to $(3 \pm 2) \times 10^{16} \text{ cm}^{-3}$ among the 200 μm diameter devices as the i layer reached the $i-n^+$ junction, at room temperature.

4. ^{55}Fe photon counting X-ray spectroscopy

4.1. Measurements with an ^{55}Fe radioisotope X-ray source

X-ray spectra were accumulated using representative 200 μm and 400 μm diameter devices to characterize their X-ray detection performance. An ^{55}Fe radioisotope X-ray source was positioned 5 mm above the top of the device under test. Each device was

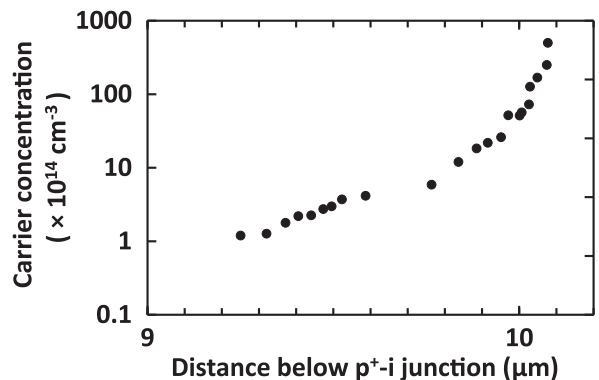


Fig. 8. Calculated carrier concentration of a representative 200 μm diameter GaAs p^+-i-n^+ photodiode at room temperature.

connected in turn to a custom made, single channel, charge sensitive preamplifier. The preamplifier was of a feedback resistorless design, similar to Ref. [28], and had a Vishay Siliconix 2N4416 JFET as the input transistor. The output signal of the preamplifier was shaped and amplified using an Ortec 572A shaping amplifier. Digitization was achieved using an Ortec EASYMCA multi channel analyzer (MCA). The live time for each obtained spectrum was 180 s.

X-ray spectra were obtained for both devices at the optimum shaping time for the currently reported GaAs detector-preamplifier system, which was found to be 10 μ s and at a range of applied reverse biases, from -5 V to -30 V with a 5 V step. The detected ^{55}Fe photopeak was the combination of the characteristic lines of the ^{55}Fe radioisotope X-ray source: Mn K α at 5.9 keV and Mn K β at 6.49 keV [29]. Gaussians were fitted to the detected photopeak taking into account the relative emission ratio [29] and the relative efficiency of the detectors for the 5.9 keV and the 6.49 keV peaks. The position of the zero energy noise peak and the position of the fitted Mn K α peak were used for the energy calibration of each spectrum. The best energy resolution (*FWHM* at 5.9 keV) of each device was achieved at -5 V reverse bias; 625 eV and 740 eV for the 200 μ m and the 400 μ m diameter device, respectively.

Fig. 9 shows the obtained ^{55}Fe spectra with the 200 μ m and 400 μ m diameter device both at -5 V reverse bias, 10 μ s shaping time and at room temperature. The counts of the zero energy noise peak were limited by setting the MCA low energy cut-off at 0.8 keV and at 1.0 keV for the 200 μ m (Fig. 9a) and the 400 μ m (Fig. 9b) diameter device respectively. However, a small portion of

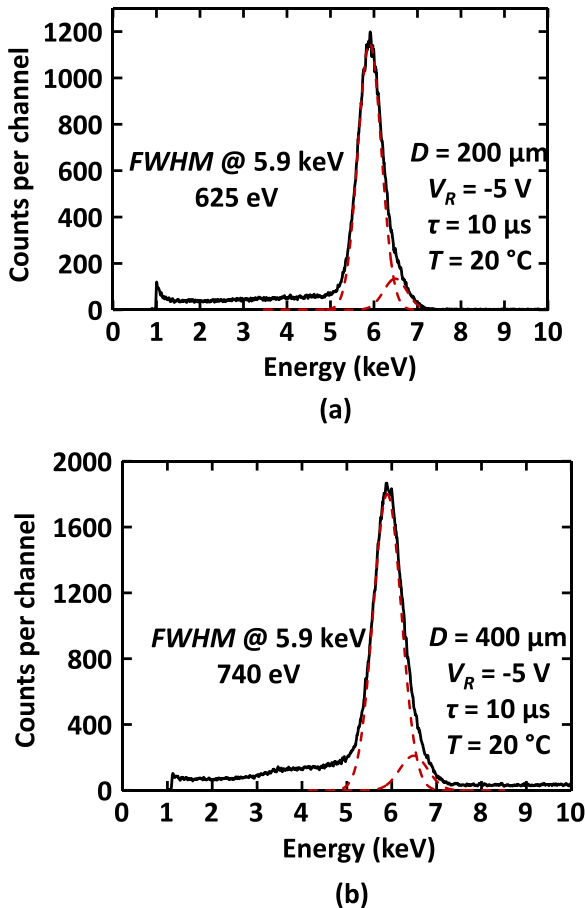


Fig. 9. ^{55}Fe spectra accumulated with (a) a 200 μ m and (b) a 400 μ m diameter GaAs p^+-i-n^+ photodiode at -5 V reverse bias, 10 μ s shaping time and room temperature along with the fitted Mn K α and K β peaks (dashed lines).

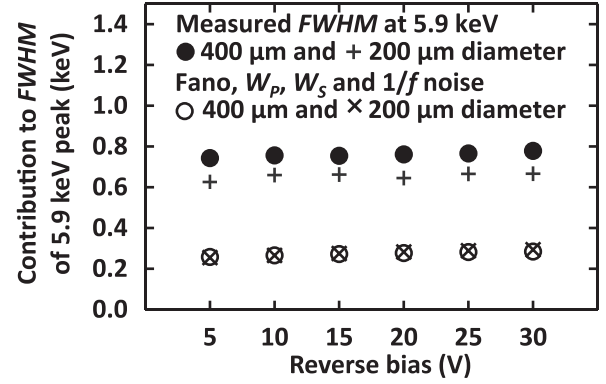


Fig. 10. Total measured *FWHM* at 5.9 keV for the 200 μ m (+ symbol) and 400 μ m (filled circles) diameter devices with the calculated Fano noise, white parallel noise, W_p , white series noise, W_s and $1/f$ noise (readily calculated electronic noise components) for the 200 μ m (\times symbol) and 400 μ m (open circles) diameter device as a function of applied reverse bias, at 10 μ s and room temperature.

the right hand side of the zero energy noise peak of the pre-amplifier can be seen in Fig. 9a. The low energy tailing of the photopeak was attributed to possible partial charge collection of charge created in the non-active layers of the devices, similarly to Refs. [21,30]. The valley-to-peak (V/P) ratios were 0.030 and 0.034, for the 200 μ m (Fig. 9a) and the 400 μ m (Fig. 9b) diameter device respectively.

4.2. Noise analysis

The *FWHM* of the 5.9 keV peak was measured for all obtained spectra and can be seen in Fig. 10 as a function of applied reverse bias, for both devices at 10 μ s and room temperature. The *FWHM* of the 5.9 keV peak was found to slightly increase from 625 eV at -5 V reverse bias to 665 eV at -30 V reverse bias for the 200 μ m diameter device. Similarly, the *FWHM* of the 5.9 keV peak was found to increase from 740 eV at -5 V reverse bias to 780 eV at -30 V reverse bias for the 400 μ m diameter device. Explanation of this increase in *FWHM* at greater reverse biases requires discussion of the noise sources affecting the resolution of the photo-peak.

There are three noise components which affect the energy resolution of any non-avalanche semiconductor X-ray spectrometer [31]. These are the Fano noise, F_N , the electronic noise, A , and the incomplete charge collection noise, R . The Fano noise is the result of the statistical nature of the ionization process [32] and can be calculated for each X-ray photon energy given that the Fano factor, F , and the electron hole pair creation energy, ω , of the semiconductor material are known. Given a Fano factor of 0.12 [33] and an electron hole pair creation energy of 4.184 eV [1] for GaAs, the Fano noise was calculated to be 128 eV at 5.9 keV. The electronic noise is a result of the detector itself and the preamplifier. It comprises of white parallel noise, W_p , white series noise, W_s , $1/f$ noise and dielectric noise, D [34]. Incomplete charge collection noise is a result of carrier trapping (charge trapping noise) and recombination in the low field region (partial charge collection noise). The quadratic sum of all the noise sources gives the total energy resolution of the system.

Along with the Fano noise, the white parallel noise, the white series noise and the $1/f$ noise can be directly calculated [34]. The white series noise, due to the capacitance of the detector and input JFET, is inversely proportional to the shaping time, the white series noise, due to the leakage current of the detector and the input JFET, is directly proportional to the shaping time and lastly, the $1/f$ noise is independent of shaping time [35]. The quadratic sum of the Fano noise and the readily calculated electronic noise components (W_p , W_s and $1/f$) was calculated for both the 200 μ m and the 400 μ m

diameter device as functions of applied reverse bias at 10 μ s shaping time and room temperature, and can be seen in Fig. 10. It was found to increase slightly from 254 eV at -5 V reverse bias to 293 eV at -30 V reverse bias for the 200 μ m diameter device and from 257 eV at -5 V reverse bias to 284 eV at -30 V reverse bias for the 400 μ m diameter device, all at 10 μ s.

Since the white parallel noise is dominant over the white series noise contribution at long shaping times, the increase in the total measured *FWHM* of the 5.9 keV peak as the reverse bias increased from -5 V to -30 V, shown in Fig. 10, was expected and was in agreement with the increase of the quadratic sum of the Fano noise and the readily calculated electronic noise components as the reverse bias increased. Although the 400 μ m diameter device capacitance (2.1 pF for $|V_R| \geq 5$ V) was greater than that for the 200 μ m device (1.1 pF for $|V_R| \geq 5$ V), the contribution of the white series noise was less significant at 10 μ s compared to the contribution of the white parallel noise (4.9 pA and 5.8 pA at -30 V reverse bias for the 400 μ m and 200 μ m diameter device respectively), resulting in similar quadratic sums of Fano, white parallel, white series, and $1/f$ noise at all reverse biases for both devices.

The difference between the measured *FWHM* at 5.9 keV and the calculated quadratic sum of the Fano and the readily calculated electronic noise components (W_s , W_p and $1/f$) was attributed to dielectric noise, D , (due to lossy dielectrics at the proximity of the input of the preamplifier [35]) and incomplete charge collection noise, R . The quadratic sum of the dielectric and incomplete charge collection noise was calculated for both the 200 μ m and the 400 μ m diameter device as functions of applied reverse bias at 10 μ s shaping time and room temperature, and can be seen in Fig. 11. It was found to be independent of shaping time with an average of (590 ± 20) eV for the 200 μ m and of (710 ± 20) eV for the 400 μ m diameter device, respectively. The non-dependence of the quadratic sum of the dielectric and charge trapping noise with the applied reverse bias suggested that the contribution of the charge trapping noise was insignificant. The dielectric noise was expected to be independent of the applied reverse bias for $|V_R| \geq 5$ V, since the dielectric noise is proportional to the capacitance of the lossy dielectrics [35] and the capacitances of both devices are independent of the reverse bias for the same range. The charge trapping noise was expected to vary with detector reverse bias. Increased reverse bias can result in less trapping noise due to improved charge transport. Hence, it may be assumed that even at -5 V reverse bias, there was no significant charge trapping noise. Consequently, it can be said that there was (590 ± 20) eV and (710 ± 20) eV dielectric noise when the 200 μ m and the 400 μ m diameter device was used respectively. The higher dielectric noise of the 400 μ m diameter device-preamplifier system compared to the 200 μ m diameter device-preamplifier system

was attributed to the higher capacitance of the 400 μ m diameter device.

To conclude, both devices had similar quadratic sums of Fano, white parallel, white series, and $1/f$ noise at all reverse biases at 10 μ s, as can be seen in Fig. 10, but the higher capacitance of the 400 μ m diameter device than that of the 200 μ m diameter device resulted in higher dielectric noise in the 400 μ m diameter spectrometer compared to that of the 200 μ m diameter spectrometer. The total outcome was a better resolution (*FWHM* at 5.9 keV) using the 200 μ m diameter device in comparison with the 400 μ m device. The energy resolution of the 200 μ m $p^+ - i - n^+$ mesa photo-diodes reported here (625 eV) is the best reported for this type of device, but is not as good as the best experimental reports of GaAs $p^+ - i - n^+$ structures grown on a semi-insulating substrates with Schottky contacts. Erd et al. reported 300 eV *FWHM* at 5.9 keV [18] and Owens et al. reported 266 eV *FWHM* at 5.9 keV [2,17], both at room temperature. These very good performance was attributed to ultra low noise read out electronics used. In both cases, the detector and the input JFET of the preamplifier were mounted on the same low-loss substrate [2,18] which is believed to reduce the dielectric noise contribution. The dielectric noise may be the main source of noise limiting the spectral resolution of the currently reported system. However, the best energy resolution of the 200 μ m device reported here (625 eV) is better than previously reported results for same diameter, thinner devices (745 eV *FWHM* at 5.9 keV for a 7 μ m i layer [21] and ≈ 800 eV *FWHM* at 5.6 keV for 3 μ m i layer [20]), coupled to similar front end electronics, possible due in part to the lower capacitance of the 200 μ m diameter device compared to those previously reported which resulted in less W_s , $1/f$ and dielectric noise contributions and improved GaAs material quality.

5. ^{63}Ni β^- particle spectroscopy

A ^{63}Ni (endpoint energy = 66 keV) β^- particle spectrum was acquired using the 200 μ m diameter device, in order to investigate its use for β^- particle and electron counting spectroscopy. Electron absorption in the device was first simulated using the computer program CASINO [36,37], the results of which are presented below. Subsequently, the accumulated ^{63}Ni spectrum is shown and the results are discussed based on the simulations and the accepted ^{63}Ni β^- spectrum.

5.1. CASINO simulations

The computer program CASINO allows Monte Carlo simulations of electrons interacting with solids [36,37]. More specifically, the trajectories of electrons while they pass through a material can be calculated in three spatial dimensions. Such simulations give an indication of how the structure of the device (thickness of dead layers and active layers) affects the total energy detected (deposited in the active layer) at the device. The geometry of the detector was defined in CASINO with the structure shown in Table 1. Since the top Ohmic contact covered 45% of the face of the 200 μ m diameter device (55% of the face being open to illumination), simulations were carried out for situations without and with the contact to cover both cases. The inactive Nickel overlayer (~ 1 μ m) covering the ^{63}Ni radioisotope β^- particle source was also included in the simulations as was the N_2 (air) layer (5 mm) between the ^{63}Ni radioisotope β^- particle source and the top of the detector.

A total of 4000 electrons were simulated with energies from 1 keV to 66 keV, forming a point source at the face of the device for simplicity. The simulated electrons had energies from 1 keV to 66 keV (the ^{63}Ni endpoint energy), with a step of 1 keV. The

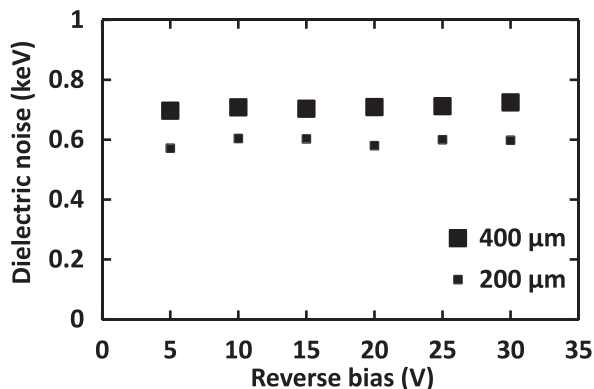


Fig. 11. Calculated quadratic sum of the dielectric and incomplete charge collection noise for the 200 μ m (small filled squares) and the 400 μ m (large filled squares) device as a function of applied reverse bias at 10 μ s and at room temperature.

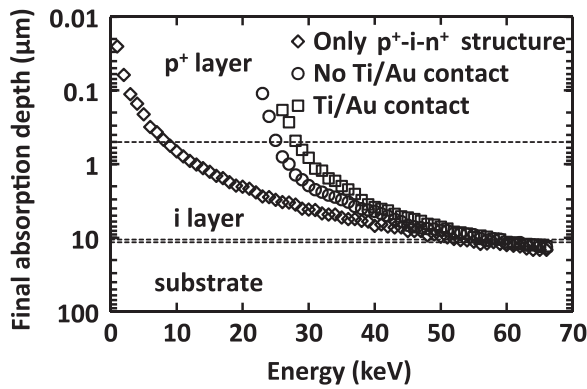


Fig. 12. Calculated final absorption depth of electrons in the GaAs p^+-i-n^+ device as a function of their energy. All layers of the GaAs p^+-i-n^+ device (p^+ , i , n^+ and substrate) are also included. n^+ layer, between i layer and substrate is not labeled on the figure for clarity.

maximum depths to which electrons of specific energy can penetrate before being completely absorbed in the device, both when they were not interacting with the top Ti/Au contact (55% of the area of the face of the 200 μm diameter device) and when they were interacting with the top Ti/Au contact (45% of the area of the face of the 200 μm diameter device), were calculated using CASINO and can be seen in Fig. 12 as a function of electrons energy. To explore the attenuating effects of the inactive Nickel overlayer of the source in addition to the air and contacts, the final absorption depth of the simulated electrons as a function of their energy when only the p^+-i-n^+ structure was taken into account (i.e. no inactive Nickel overlayer, air or Ti/Au contacts) and thus p^+ layer being the only dead layer, is also presented in Fig. 12.

The electrons lose their energy along their path through the device. A percentage of the particle energy incident on the device was deposited in the dead layers reducing the total particle energy deposited in the active i layer, therefore reducing the energy detected. The total energy of particles up to 25 keV, when not passing through the Au/Ti top Ohmic contact, and the total energy of particles up to 28 keV, when passing through the Au/Ti top Ohmic contact was absorbed within the top dead layers (i.e. inactive Ni overlayer, air, contacts and p^+ layer). A percentage of the electrons with energies equal to and higher than 60 keV (for both including and not including the Au/Ti top Ohmic contact) were also absorbed in the n^+ layer/substrate reducing the available particle energy being deposited at the active layer. More specifically, it was found that 0.1% (for 60 keV) to 1.4% (for 66 keV) of electrons, when interacting with the top contact, deposited part of their energy in the n^+ layer/substrate. Similarly, it was found that 0.2% (for 60 keV) to 1.7% (for 66 keV) of electrons, when they were not interacting with the top contact, deposited part of their energy in the n^+ layer/substrate. The maximum depth of the 66 keV electrons (^{63}Ni endpoint energy) was found to be 13.5 μm and 13 μm when they were not passing through and when they were passing through the top contact, respectively.

For electrons or β^- particles impinging directly on top of the p^+-i-n^+ photodiode (i.e. no Nickel overlayer, air and Ti/Au contacts were taken into account), it was found that only particles of energy less than 8 keV were not reaching the active i layer (Fig. 12). Particles of energy greater than 53 keV lost part of their energy in the n^+ layer/substrate, with the 66 keV β^- particles reaching a maximum depth of 14.5 μm . The elimination of the inactive nickel overlayer of the ^{63}Ni radioisotope β^- particle source and the air gap between the source and the top of the device along with a reduction of the thickness of the p^+ layer, from 0.5 μm to ideally 0 nm (assuming the entire p^+ layer were inactive, which is pessimistic) and an increase in the thickness of

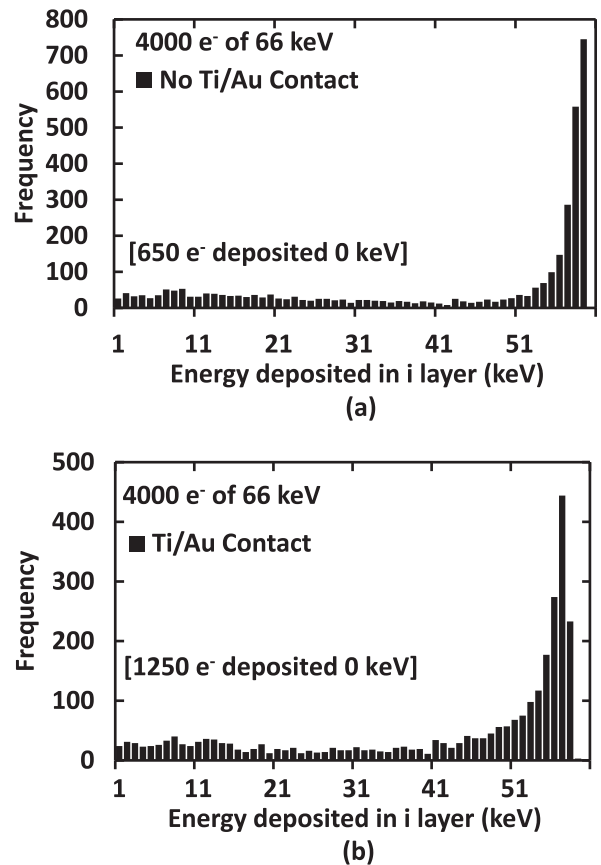


Fig. 13. Calculated distribution of total energy deposited in i layer of 4000 66 keV electrons when (a) not interacting and (b) interacting with the Ti/Au top Ohmic contact which covered 45% of the face of the GaAs p^+-i-n^+ photodiodes.

the i layer, from 10 μm to 14.5 μm , would result in the deposition of the total β^- particle energy in the active layer and hence to the detection of all β^- particles emitted from the ^{63}Ni radioisotope β^- particle source. The fact that these criteria were not fulfilled, together with the simulation results discussed below, explain the apparent endpoint energy observed in the experimental measurements presented in Section 5.2.

The calculated trajectories of 4000 electrons each having an energy of 66 keV were also used to calculate the energy being deposited in the i layer. Similarly to the previous CASINO simulations, electrons were simulated for both occasions where the electrons were incident on the top Ohmic contact and where the electrons were incident on the optical window of the detector. For both cases, the distribution of particle energy deposited in the i layer for 4000 electrons each of energy 66 keV, is presented in Fig. 13.

CASINO simulations showed that the most probable (18.6% of electrons simulated) amount of energy deposited in the i layer by 66 keV electrons incident on the optical window of the detector was 59 keV (Fig. 13a), with the maximum energy being 60 keV (0.05%). It was also found that a total of 16.2% (650 out of 4000) of the electrons were fully absorbed before reaching the i layer and thus not detected at all. When the same electrons were simulated as incident upon the top Ohmic contact, it was found that the maximum energy deposited in i layer was reduced to 59 keV, with the most probable energy (31.2%) deposited being 0 keV, followed by 57 keV (11.1%) (Fig. 13b). Hence, a 66 keV β^- particle emitted from the ^{63}Ni β^- particle source can deposit in i layer of the GaAs p^+-i-n^+ photodiode energy totaling between 0 keV and 60 keV, depending on its three dimensional trajectory. Defining the external quantum efficiency (EQE) as the ratio of the total energy

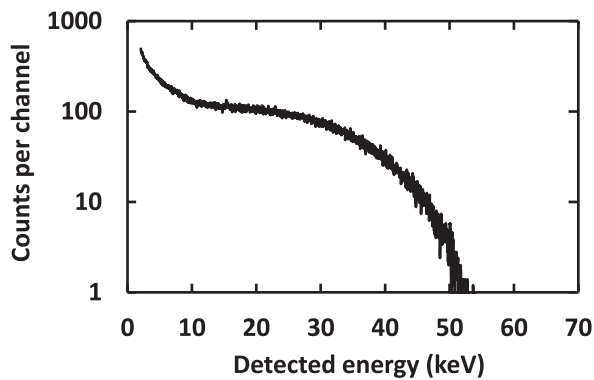


Fig. 14. ^{63}Ni β^- spectrum obtained with a 200 μm diameter GaAs $\text{p}^+\text{-i-n}^+$ photodiode at 2 μs shaping time, 10 V reverse bias and at room temperature.

deposited at the i layer by the total energy emitted from the ^{63}Ni β^- particle source, an EQE of 49% at 66 keV was calculated for the currently reported electron photodiode spectrometer, limited by the absorption of electrons (β^- particles) in the top dead layers (Nickel overlayer, air, Ti/Au contacts and p^+ layer).

5.2. ^{63}Ni β^- particle spectra and discussion

The ^{63}Ni radioisotope β^- particle source was positioned 5 mm above the top of the 200 μm diameter GaAs $\text{p}^+\text{-i-n}^+$ photodiode. Due to a different front end configuration of the preamplifier to accommodate the ^{63}Ni source, the optimum shaping time for the system shortened to 2 μs . The detector was reverse biased at 10 V throughout the accumulation (live time limit=400 s). A low energy threshold of 2 keV was set to minimize counts from the zero energy noise peak. The accumulated ^{63}Ni β^- spectrum is presented in Fig. 14. The spectrum was energy calibrated using the energy calibration derived from ^{55}Fe radioisotope X-ray source (Mn $\text{K}\alpha=5.9$ keV; Mn $\text{K}\beta=6.49$ keV) measurements under the same conditions (shaping time, reverse bias and temperature). It should be noted that the zero energy noise peak in the accumulated ^{63}Ni radioisotope β^- particle spectrum was not entirely eliminated by the low energy threshold; the right hand side of its tail can still be seen in Fig. 14 due to additional capacitive and dielectric effects being introduced by the presence of the source [23].

The events which comprise the spectrum shown in Fig. 14 have detected energies equal to those deposited in the active layer of the device. As was discussed in Section 5.1, the energy deposited by each β^- particle in the active layer of the device is different from its initial energy and dependent upon its initial energy and track through the detector. The apparent endpoint energy measured with the device was ~ 50 keV, which is lower than the accepted endpoint energy of the ^{63}Ni β^- spectrum. It suggested that 75% of the 66 keV particle energy was deposited at the active i layer whilst the rest was deposited at the top dead layers and n^+ layer/substrate. As was discussed in Section 5.1, this was due in part to the inactive nickel overlayer of the ^{63}Ni radioisotope β^- particle source, attenuation in the air, as well to as attenuation in the inactive p^+ layer of the detector. This is in accordance with the simulations which showed that the energy deposited in i layer of the GaAs $\text{p}^+\text{-i-n}^+$ photodiode from a 66 keV β^- particle emitted from the ^{63}Ni β^- particle source can range between 0 keV and 60 keV, depending on its trajectory.

Although the GaAs devices reported here were not specifically designed for β^- or electron spectroscopy, Fig. 14 shows that they can be used for counting β^- particles and measuring the total energy being deposited in the active region of the detectors. The limiting factor of the devices for β^- particle detection was found

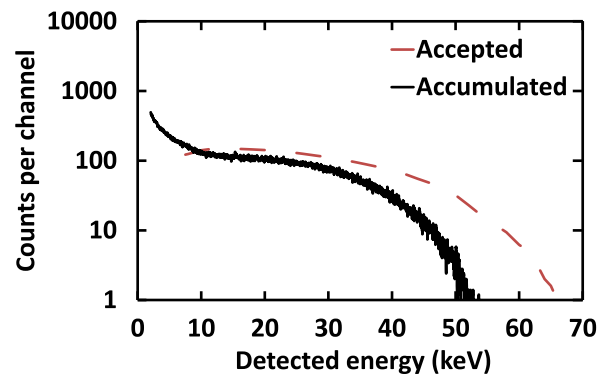


Fig. 15. Accumulated ^{63}Ni β^- spectrum (solid line) and accepted shape of the ^{63}Ni β^- spectrum (dashes) as reported by Preiss et al. [38].

to be the thickness of the p^+ layer which reduced the total β^- particle energy being absorbed in the active layer. Fig. 15 shows the accepted shape of the ^{63}Ni β^- spectrum as reported by Preiss et al. [38] along with the accumulated ^{63}Ni β^- spectrum using the 200 μm diameter GaAs photodiode. Preiss et al.'s data have been normalized to the accumulated spectrum to reflect the different count rates and accumulation times.

6. Conclusions and future work

A total of 22 randomly selected GaAs $\text{p}^+\text{-i-n}^+$ mesa X-ray photodiodes have been electrically characterized at room temperature with two representative diodes being further characterized as detectors for photon counting X-ray spectroscopy and one of the diodes for β^- particle counting spectroscopy. The devices had a 10 μm thick i layer. There were 14 diodes with 200 μm diameters and 8 diodes with 400 μm diameters.

The ideality factor, which was found to vary from 1.89 to 1.99 among different devices with a mean of 1.95 ± 0.02 , indicated that the recombination current defined the forward current. Low leakage current densities were measured for all devices at room temperature, at an applied electric field of 50 kV/cm: it was found to vary from 4 nA/cm² to 67 nA/cm² among all diodes (both 200 μm and 400 μm diameter devices) with an average of (30 ± 20) nA/cm². The 400 μm diameter devices showed lower leakage current densities than the 200 μm diameter devices at 50 kV/cm, suggesting that the surface leakage current was not negligible, possibly due to the devices being unpassivated.

The i layer thickness and doping concentration of the devices were deduced from capacitance measurements. All the diodes were almost fully depleted at 0 V. The depletion width of the 400 μm diameter devices was found to increase from 9.9 ± 0.2 μm at 0 V to 10.6 ± 0.2 μm at 50 V. The depletion width the 200 μm diameter devices was determined to be 10 ± 1 μm at 0 V and 11 ± 1 μm at 50 V. The unintentional doping density of the i layer was found to be $(2.8 \pm 0.9) \times 10^{14}$ cm⁻³ for the 400 μm diameter devices and $(0.8 \pm 0.4) \times 10^{14}$ cm⁻³ for the 200 μm diameter devices.

Results demonstrating the devices' performance as room temperature X-ray spectrometers with an ^{55}Fe radioisotope X-ray source were reported as functions of applied reverse bias at 10 μs shaping time. The best energy resolution (FWHM at 5.9 keV) was achieved at -5 V reverse bias for both the 200 μm and a 400 μm diameter devices. The FWHM was found to increase from 625 eV at -5 V reverse bias to 665 eV at -30 V reverse bias for the 200 μm diameter detector. Similarly, the FWHM of the 5.9 keV peak was found to increase from 740 eV at -5 V reverse bias to 780 eV at -30 V reverse bias for the 400 μm diameter detector. Noise

analysis showed that the dominant source of noise of the currently reported system was the dielectric noise. It was calculated to be (590 ± 20) eV and (710 ± 20) eV when the 200 μm and the 400 μm diameter devices, respectively, were used.

A ^{63}Ni (endpoint energy = 66 keV) β^- spectrum was obtained with the 200 μm diameter device to characterize the GaAs photodiodes as electron detectors. CASINO simulations showed that the layers between the active ^{63}Ni and detector (i.e. inactive Nickel overlayer of the ^{63}Ni radioisotope β^- particle source and 5 mm of air) and the inactive layers at the front of the detector (annular Ti/Au contact and p^+ layer) limited the total energy being deposited at the active layer of the device. Simulations showed that β^- particles with an energy of 25 keV impinging on the optical window of the detector (28 keV when impinging on the top Ohmic contact) were all absorbed before reaching the active i layer. Also, a percentage of β^- particles with an energy higher than 60 keV was absorbed in the n^+ layer/substrate. CASINO simulations at the endpoint energy of the ^{63}Ni β^- source revealed that the detected energy of 66 keV β^- particles can range from 0 keV to 60 keV, depending on their track. The accumulated spectrum had an apparent endpoint energy of 50 keV which suggested that 75% of the 66 keV particle energy was deposited at the active i layer. Although the GaAs devices reported here were not specifically designed for β^- or electron spectroscopy, it can be concluded that they can be used for counting β^- particles (electrons) and measuring the total energy being deposited in their active region.

Future work includes characterization of the devices at high temperatures as well as characterization of thicker devices having higher quantum efficiency. The elimination of the parasitic dielectrics using the same low-loss substrate for the detector and the input JFET of the preamplifier is also part of the future work and is expected to further improve the resolution of the system.

Authors' Data Statement

Data underlying this work are subject to commercially confidentiality. The Authors regret that they cannot grant public requests for further access to any data produced during the study, however the key findings are fully included within the article.

Acknowledgments

This work was supported in part by STFC Grant nos. ST/M002772/1 and ST/M004635/1 and Royal Society Grant no. RS130515. The authors are grateful to B. Harrison, R. J. Airey and S. Kumar at the EPSRC National Centre for III-V Technologies for material growth and fabrication. G. Lioliou acknowledges funding received in the form of PhD scholarship from University of Sussex.

References

- [1] G. Bertuccio, D. Maiocchi, J. Appl. Phys. 92 (2002) 1248.
- [2] G. Bertuccio, R. Casiraghi, D. Maiocchi, A. Owens, M. Bavdaz, A. Peacock, H. Andersson, S. Nenonen, IEEE Trans. Nucl. Sci. 50 (2003) 723.
- [3] A. Šagátová, B. Zaťko, M. Pavlovič, K. Sedláčková, P. Hybler, F. Dubecký, V. Nečas, J. Instrum. 9 (2014) C04036.
- [4] V.K. Dixit, S.K. Khamari, S. Manwani, S. Porwal, K. Alexander, T.K. Sharma, S. Kher, S.M. Oak, Nucl. Instrum. Methods Phys. Res. Sect. A 785 (2015) 93.
- [5] L. Rossi, P. Fischer, T. Rohe, N. Wermes, Pixel Detectors: From Fundamentals to Applications, Springer, Berlin Heidelberg, 2006.
- [6] E.A. Kolawa, E.E. Technologies Study Team, Extreme Environment Technologies for Future Space Science Missions. Technical Report JPL D-32832, National Aeronautics and Space Administration, Washington D.C., 2007.
- [7] F. Bagenal, T.E. Dowling, W.B. McKinnon, Jupiter the Planet, Satellites and Magnetosphere, Cambridge University Press, Cambridge, 2004.
- [8] A. Atzei, A. Wielders, A. Stankov, P. Falkner, Overview of the ESA Jovian technology reference studies, Technical Note, ESA/ESTEC, The Netherlands, 2007.
- [9] L. Roth, J. Saur, K.D. Retherford, D.F. Strobel, P.D. Feldman, M.A. McGrath, F. Nimmo, Science 343 (2014) 171.
- [10] G.F. Knoll, Radiation Detection and Measurements, 3rd ed., John Wiley & Sons, New York, 2000.
- [11] C. Celik, J. Radioanal. Nucl. Chem. 292 (2012) 1317.
- [12] N. Tsoulfanidis, Measurements and Detection of Radiation, 2nd ed., Taylor & Francis, Washington, 1995.
- [13] C. Grupen, I. Buvat, Handbook of Particle Detection and Imaging, Springer-Verlag, Berlin Heidelberg, 2012.
- [14] D.R. Linder, A.J. Coates, R.D. Woodliffe, C. Alsop, A.D. Johnstone, M. Grande, A. Preece, B. Narheim, D.T. Young, The Cassini CAPS Electron Spectrometer in Measurement Techniques in Space Plasmas: Particles, American Geophysical Union, Washington, 1998.
- [15] R. Bedington, D. Kataria, D. Walton, J. Instrum. 7 (2012) C01079.
- [16] J. Gruenewald, D. Tskhakaya, J. Kovačič, M. Čerček, T. Gyergyek, C. Ionita, R. Schrittwieser, Plasma Sources Sci. Technol. 22 (2013) 015023.
- [17] A. Owens, M. Bavdaz, A. Peacock, A. Poelaert, H. Andersson, S. Nenonen, H. Sipilä, L. Tröger, G. Bertuccio, J. Appl. Phys. 90 (2001) 5376.
- [18] C. Erd, A. Owens, G. Brammertz, M. Bavdaz, A. Peacock, V. Lämä, S. Nenonen, H. Andersson, N. Haack, Nucl. Instrum. Method. Phys. Res. Sect. A 487 (2002) 78.
- [19] A.M. Barnett, J.E. Lees, D.J. Bassford, J.S. Ng, C.H. Tan, N. Babazadeh, R.B. Gomes, Nucl. Instrum. Method. Phys. Res. Sect. A 654 (2011) 336.
- [20] A.M. Barnett, Nucl. Instrum. Method. Phys. Res. Sect. A 756 (2014) 39.
- [21] G. Lioliou, X. Meng, J.S. Ng, A.M. Barnett, Nucl. Instrum. Method. Phys. Res. Sect. A 813 (2016) 1.
- [22] G. Lioliou, X. Meng, J.S. Ng, A.M. Barnett, J. Appl. Phys. 119 (2016) 124507.
- [23] A.M. Barnett, J.E. Lees, D.J. Bassford, J. Instrum. 7 (2012) P09012.
- [24] S. Butera, G. Lioliou, A.M. Barnett, J. Appl. Phys. 119 (2016) 064504.
- [25] S.M. Sze, Physics of Semiconductor Devices, 3rd ed., John Wiley & Sons, New Jersey, 2007.
- [26] J.S. Ng, X. Meng, J.E. Lees, A. Barnett, C.H. Tan, J. Instrum. 9 (2014) T08005.
- [27] M. Takenaka, K. Morii, M. Sugiyama, Y. Nakano, S. Takagi, Opt. Express 20 (2012) 8718.
- [28] G. Bertuccio, P. Rehak, D. Xi, Nucl. Instrum. Method. Phys. Res. Sect. A 326 (1993) 71.
- [29] U. Schötz, Appl. Radiat. Isot. 53 (2000) 469.
- [30] A.M. Barnett, G. Lioliou, J.S. Ng, Nucl. Instrum. Method. Phys. Res. Sect. A 774 (2015) 29.
- [31] G.W. Fraser, X-Ray Detectors in Astronomy, Cambridge University Press, Cambridge, 1989.
- [32] G. Bertuccio, IEEE Solid-State Circuits Mag. 4 (2012) 36.
- [33] G. Bertuccio, A. Pullia, J. Lauter, A. Forster, H. Luth, IEEE Trans. Nucl. Sci. 44 (1997) 1.
- [34] G. Lioliou, A.M. Barnett, Nucl. Instrum. Method. Phys. Res. Sect. A 801 (2015) 63.
- [35] G. Bertuccio, A. Pullia, G. De Geronimo, Nucl. Instrum. Method. Phys. Res. Sect. A 380 (1996) 301.
- [36] P. Hovington, D. Drouin, R. Gauvin, Scanning 19 (1997) 1.
- [37] D. Drouin, P. Hovington, R. Gauvin, Scanning 19 (1997) 20.
- [38] I.L. Preiss, R.W. Fink, B.L. Robinson, J. Inorg. Nucl. Chem. 4 (1957) 233.